Steel and Composite Structures, *Vol. 54, No. 3 (2025) 241-250*
https://doi.org/10.12989/scs.2025.54.3.241

Crack propagation in functionally graded porous plates by enriched Petrov-Galerkin natural element method

J.R. Cho*

Department of Naval Architecture and Ocean Engineering, Hongik University, Sejong 30016, Korea

(Received July 10, 2024, Revised January 9, 2025, Accepted January 16, 2025)

Abstract. Enriched meshfree methods have been effectively used to predict the stress intensity factors (SIFs) and crack trajectories for homogeneous structures, but their applications to heterogenous materials were rarely reported. In this context, an enriched Petrov-Galerkin natural element method (PG-NEM) is introduced to simulate and examine the crack growth in 2-D heterogeneous functionally graded (FG) porous plates. The global displacement is approximated using Laplace interpolation (L/I) functions and enriched by introducing the crack-tip singular displacement and stress fields. The mixed-mode SIFs of FG plates characterized by the spatially varying elastic modulus are computed by the modified interaction integral method, and the crack trajectories are predicted by the maximum principal stress (MPS) criterion and the equivalent mode-I SIF. The advantage of proposed method is verified by comparing with the unriched PG-NEM and ANSYS. It is found that the prediction accuracy in crack trajectory is remarkably improved such that the crack trajectory of present method coincides well with one of ANSYS. Moreover, the present enriched method successfully simulates the crack trajectories of FG plates with the porosity as well as the spatially varying elastic modulus, and it is found that the crack growth characteristics are remarkably influenced by these parameters.

Keywords: 2-D enriched PG-NEM; crack growth length; crack propagation trajectory; crack propagation; exponentially varying elastic modulus; functionally graded porous plates; porosity distribution

1. Introduction

In 1980s, a new material notion called functionally graded material (FGM) was introduced to overcome the fatal problem of traditional bi-material-type heat-proof composites (Miyamoto *et al.* 2013, Van Do *et al*. 2022). A sharp jump in the material property distribution across the lamina interface causes the thermal stress concentration which frequently triggers the crucial problems like the interface debonding. But, this critical stress concentration could be fortunately suppressed by introducing a graded layer between two distinct material layers (Giannakopolus *et al.* 1995, Cho and Oden 2000). Since the graded layer becomes 100% base materials at the upper and lower surfaces, the sharp material discontinuity at the layer interface does not occur any more. Besides the continuity of material property, the graded layer provides the functionality for maximizing the target performance (Reiter and Dvorak 1998, Apalak 2014, Ding and Wu 2018). The material distribution within the graded layer can be designed in the direction for improving the target performance. Meanwhile, FGMs are not homogeneous but highly heterogeneous because the effective material properties vary point by point within the graded layer.

By virtue of this merit, the notion of FGM has been rapidly expanded to various engineering fields (Zhang *et al*. 2004, Yahia *et al.* 2015, Abdelaziz *et al*. 2017, Bouderba *et al.* 2018, Duc and Minh 2021, Kumar *et al*. 2023, Pham *et al.* 2023.). The major thermo-mechanical behavior of FGMs is characterized by the properties, volume fractions, size and orientation, and microstructure of constituent particles. Thus, in early days, the studies of FGMs focused on the material property estimation, the modeling and analysis for investigating the behaviors (Cho and Ha 2001; Birman and Byrd 2007). Due to the intensive research efforts, these research topics have been mostly settled down. Later, the research attention was directed to the crack problem because the micro-cracking triggers the structural failure of FGMs (Mahamood *et al.* 2012, Ivanov *et al.* 2013). Hence, the crack-tip stress distribution, SIFs and the crack growth have been emerged as the hot research issues (Dolbow and Gosz 2002, Tilbrook *et al.* 2005; Minh and Duc 2021, Khiem and Huong 2023). For the numerical studies of these issues, the assurance of numerical accuracy is essential because the crack-tip stress field shows the $1/\sqrt{r}$ singularity (Delale and Erdogan 1983, Eischen 1987, Ayhan 2007, Nguyen *et al.* 2022).

Moreover, the heterogeneity of FGM made the numerical reliability assurance more difficult because the standard $J-$ or $M-$integral methods does not account for the position dependence of material properties. To resolve the problem of conventional methods, the numerical crack analysis of heterogeneous bodies were studied in 1970~80s. The position dependence of elastic modulus was expressed by an exponential function (Delale and Erdogan 1983, Atkinson and List 1978), and the standard integral methods were modified to reflect the position dependence

*Corresponding author, Professor
E-mail: jrcho@hongik.ac.kr

ISSN: 1229-9367 (Print), 1598-6233 (Online)

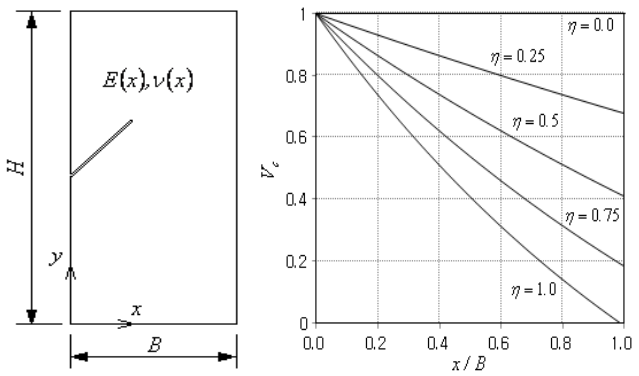

(a) (b)

Fig. 1 A cracked ceramic-metal FG plate: (a) geometry dimensions, (b) ceramic volume fraction distribution $V_c(x)$

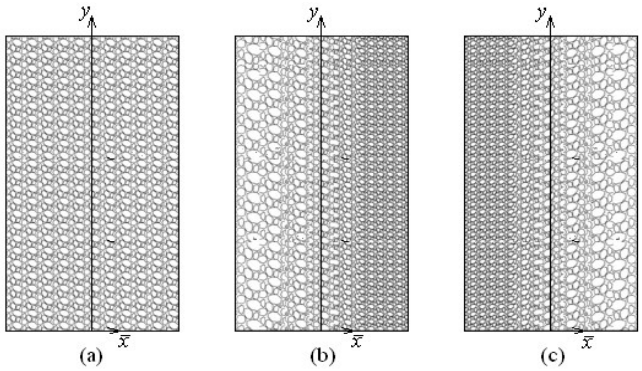

Fig. 2 Porosity distributions: (a) uniform (sym), (b) left-biased (sym-1), (c) right-biased (sym-2)

of material properties of FGM. The representative ones include the equivalent domain integral (Gu *et al.,* 1999, Nikishkov *et al.* 2016), the division of FGM domain into finite number of homogeneous sub-domains (Anlas *et al*. 2000), and the path-independent J_k^*-integral (Kim and Paulino, 2002, Zhu 2023). These refined methods were commonly developed based on the finite element method.

Regarding the meshfree method, its application to the crack problem of heterogeneous structures was initiated at the late of 1990s. Rao and Rahman (2003) and Liu *et al.* (2008) employed the meshfree methods to compute the SIFs of FGMs using the modified $M-$integral method of Gu *et al.* (1999). Cho and Lee (2014) extended NEM to the SIF computation for both homogeneous and heterogeneous materials. The NEM was introduced to remove the demerits of conventional meshfree methods in implementing the Gauss integration and the displacement boundary conditions (Sukumar *et al.* 1998, Cho and Lee 2006). NEM employs the high smooth Laplace interpolation functions to approximate the displacement field, but further enhancement is required to accurately represent the near-tip singular stress field. The enhancement is usually made by enriching the basis or interpolation functions. Then, the accuracy in approximating the crack-tip stress field predicting the SIFs and crack trajectories is improved (Fleming *et al.* 1997). Even though the effectiveness of this enrichment approach has been verified for homogeneous materials (Pant *et al.* 2013), its application to heterogeneous material has been rarely presented.

In this regard, this study aims at introducing a 2-D enriched Petrov-Galerkin NEM to simulate the crack propagation in heterogeneous material and investigating crack growth characteristics of FG porous plates with respect to the key parameters. The displacement field is approximated with L/I functions and its near-tip part is enriched by adding the crack-tip singular displacements. The approximated strain and stress files are smoothened by the strain recovery technique (Cho 2016). The mixed-mode SIFs in heterogeneous FG porous plates are calculated by employing the modified interaction integral, and the crack trajectories are obtained by combining the equivalent mode-I SIF and the MPS criterion. The proposed method is demonstrated through the numerical experiments and verified by comparing with ANSYS (2019). Moreover, the crack propagation in heterogeneous and porous FG plates is examined with regard to the elastic modulus index and the porosity distribution.

2. Ceramic-metal FG porous plates

Fig. 1(a) represents a cracked inhomogeneous rectangular plate of width B and height H in which ceramic and metal particles are functionally distributed in the horizontal direction. Denoting $V_c(x)$ and $V_m(x)$ be the ceramic and metal volume fractions, both satisfy

$$V_c(x)+V_m(x)=1, \quad 0\le x\le B \tag{1}$$

Due to this physical relation, either of the two is enough to identify the material composition within the plate. In this study, the ceramic volume fraction is chosen and assumed to vary as

$$V_c(x)=\frac{2}{exp(0.7\eta x/B)}-1, \quad \eta>1.0 \tag{2}$$

The left side of plate becomes ceramic while the right side becomes metal when the elastic modulus index $\eta=1$. The horizontal distributions of ceramic volume fraction $V_c(x)$ are represented in Fig. 1(b) for different values of η.

The effective elastic modulus $E(x)$ of ceramic-metal FG plate is determined by

$$\begin{aligned} E(x) &= V_c E_c + V_m E_m \\ &= E_c / exp(0.7\eta x/B) \end{aligned} \tag{3}$$

According to the linear rule of mixture (Cho and Ha 2001). In the same manner, the shear modulus, Poisson's ratio and fracture toughness are also calculated by this rule.

Next, the distribution of pores between ceramic and metal particles is assumed to be uniform, left-biased and right-biased, as represented in Fig. 2. Letting $\bar{x}$ be $(x-0.5B)/B$, three porosity distributions $\psi(\bar{x})$ is expressed as

$$\psi(\bar{x}) = \vartheta\, cos\left[\frac{\pi}{A}(\bar{x}+B)\right] \tag{4}$$

with the porosity parameter $\vartheta(0 \le \vartheta \le 1)$. In which $A = 1.0, B = 0$ for symmetric, $A = 2.0, B = 0.5$ for unsym-1, and $A = 2.0, B = -0.5$ for unsym-2, respectively.

The porosity influences the magnitudes of material properties of ceramic-metal FG plates. By referring to Phani and Niyogi (1987) and Flinn *et al.* (2000), the effective elastic modulus E and the effective fracture stiffness K_{Ic} are modified respectively as

$$E(x) = E(x)\cdot\left[1-\psi(x)\right], \quad \eta \ge 0 \tag{5}$$

$$K_{Ic}(x) = K_{Ic}(x)\cdot\left[1-\psi(x)\right]^{1.15}, \quad \eta \ge 0 \tag{6}$$

3. Linear fracture mechanics of inhomogeneous materials

This section explains the numerical methods for evaluating the mixed-mode SIFs and predicting the crack growth trajectory in heterogeneous FG structures having an edge crack. Fig. 3(a) represents the structure domain $\Omega \in \Re^2$ of cracked FG structure and its boundary $\partial\Omega = \overline{\Gamma_D \cup \Gamma_N \cup \Gamma_c}$, where Γ_D and Γ_N denote the displacement and force boundaries while $\Gamma_c = \overline{\Gamma_c^+ \cup \Gamma_c^-}$ indicates the crack top surface, respectively. The elastic modulus E is not constant but varying point by point within the structure domain. For the purpose of description convenience, two Cartesian coordinates are introduced: $\{x, y\}$ for the 2-D linearly elastic problem and $\{x', y'\}$ for the computation of mixed-mode SIFs and the prediction of crack propagation trajectory, respectively.

Letting $\boldsymbol{u}(\boldsymbol{x})$ and σ be the displacement field and Cauchy stresses respectively, the boundary value problem (BVP) is governed by the static equilibrium

$$\nabla\cdot\boldsymbol{\sigma} = 0 \quad in \quad \Omega \tag{7}$$

and the displacement and force boundary conditions given by

$$\boldsymbol{u} = \hat{\boldsymbol{u}} \quad on \quad \Gamma_D \tag{8}$$

$$\sigma\cdot\boldsymbol{n} = \begin{cases} \hat{\boldsymbol{t}} & on \quad \Gamma_N \\ 0 & on \quad \Gamma_c^{\pm} \end{cases} \tag{9}$$

Here, $\boldsymbol{n}$ denotes a unit vector outwardly normal to the boundary $\partial\Omega$ and $\hat{\boldsymbol{t}}$ denotes the external traction force.

According to Arkinson and List (1978), the $J-$integral over the integration domain A depicted in Fig. 3(b) of heterogeneous material is defined by

$$J = \int_A \left(\sigma_{\alpha\beta}\frac{\partial u_\alpha}{\partial x_1'} - W\delta_{1\beta}\right)\frac{\partial q}{\partial x_\beta'}dA - \int_A \frac{1}{2}\varepsilon_{\alpha\beta}\frac{\partial D_{\alpha\beta\gamma\delta}}{\partial x_1'}\varepsilon_{\gamma\delta}qdA \tag{10}$$

Here, $W = \sigma\cdot\varepsilon/2 = \varepsilon_{\alpha\beta}D_{\alpha\beta\gamma\delta}\varepsilon_{\gamma\delta}/2$ indicates the strain energy density with the strains $\varepsilon_{\alpha\beta}$and the elastic constants $D_{\alpha\beta}$. In Eq. (10), the weighting function $q(x)$ is defined as follows: zero on Γ_o, unity on Γ, and any value between 0 and 1 within the darkened integration region A.

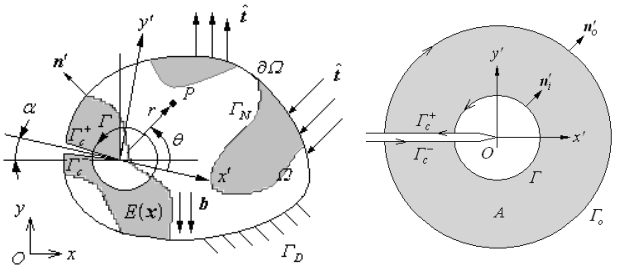

(a) (b)

Fig. 3 Representation: (a) a FG structure having an edge crack, (b) a closed loop C and a don't-like region

Next, the interaction integral in which two equilibrium states 1 and 2 of a cracked heterogeneous body is combined is adopted to compute K_I and K_{II} from the $J-$integral. The state 1 denotes the actual equilibrium state of the structure under the given boundary conditions while the state 2 indicates an auxiliary equilibrium state for which the asymptotic displacement and stress fields for modes I and II are used. And, another equilibrium state called state S is defined by combining states 1 and 2, for which the $J-$integral in Eq. (10) is written as (Rao and Rahman 2003)

$$\begin{aligned} J^{(S)} = &\int_A \left((\sigma_{\alpha\beta}^{(1)} + \sigma_{\alpha\beta}^{(2)})\frac{\partial(u_\alpha^{(1)} + u_\alpha^{(2)})}{\partial x_1'} - W^{(S)}\delta_{1\beta}\right)\frac{\partial q}{\partial x_\beta'}dA \\ &+ \int_A \frac{\partial}{\partial x_\beta'}\left((\sigma_{\alpha\beta}^{(1)} + \sigma_{\alpha\beta}^{(2)})\frac{\partial(u_\alpha^{(1)} + u_\alpha^{(2)})}{\partial x_1'} - W^{(S)}\delta_{1\beta}\right)qdA \end{aligned} \tag{11}$$

with $W^{(S)} = (\sigma_{\alpha\beta}^{(1)} + \sigma_{\alpha\beta}^{(2)})(\varepsilon_{\alpha\beta}^{(1)} + \varepsilon_{\alpha\beta}^{(2)})/2 = W^{(1)} + W^{(2)} + W^{(1,2)}$.

By virtue of the static equilibrium and the displacement-strain relations, Eq. (11) is reduced to

$$\begin{aligned} \tilde{J}^{(S)} = &\int_A \left((\sigma_{\alpha\beta}^{(1)} + \sigma_{\alpha\beta}^{(2)})\frac{\partial(u_\alpha^{(1)} + u_\alpha^{(2)})}{\partial x_1'} - (W^{(1)} + W^{(2)}\right. \\ &\left. + W^{(1,2)})\delta_{1\beta}\right)\frac{\partial q}{\partial x_\beta'}dA + \int_A \frac{1}{2}\left(-\varepsilon_{\alpha\beta}^{(1)}\frac{\partial D_{\alpha\beta\gamma\delta}}{\partial x_1'}\varepsilon_{\gamma\delta}^{(1)}\right. \\ &\left. + \sigma_{\alpha\beta}^{(1)}\frac{\partial\varepsilon_{\alpha\beta}^{(2)}}{\partial x_1'} - \frac{\partial\sigma_{\beta\beta}^{(2)}}{\partial x_1'} + \sigma_{\alpha\beta}^{(2)}\frac{\partial\varepsilon_{\alpha\beta}^{(1)}}{\partial x_1'} - \frac{\partial\sigma_{\alpha\beta}^{(1)}}{\partial x_1'}\varepsilon_{\alpha\beta}^{(2)}\right)qdA \\ &= J^{(1)} + J^{(2)} + M^{(1,2)} \end{aligned} \tag{12}$$

Here

$$\begin{aligned} J^{(1)} = &\int_A \left(\sigma_{\alpha\beta}^{(1)}\frac{\partial u_\alpha^{(1)}}{\partial x_1'} - W^{(1)}\delta_{1\beta}\right)\frac{\partial q}{\partial x_\beta'}dA \\ &-\frac{1}{2}\int_A \varepsilon_{\alpha\beta}^{(1)}\frac{\partial D_{\alpha\beta\gamma\delta}}{\partial x_1'}\varepsilon_{\gamma\delta}^{(1)}qdA \end{aligned} \tag{13}$$

$$J^{(2)} = \int_A \left(\sigma_{\alpha\beta}^{(2)}\frac{\partial u_\alpha^{(2)}}{\partial x_1'} - W^{(2)}\delta_{1\beta}\right)\frac{\partial q}{\partial x_\beta'}dA \tag{14}$$

are two $J-$integrals for states 1 and 2, and

$$\begin{aligned} M^{(1,2)} = &\int_A \left(\sigma_{\alpha\beta}^{(1)}\frac{\partial u_\alpha^{(2)}}{\partial x_1'} + \sigma_{\alpha\beta}^{(2)}\frac{\partial u_\alpha^{(1)}}{\partial x_1'} - W^{(1,2)}\delta_{1\beta}\right)\frac{\partial q}{\partial x_\beta'}dA \\ &+ \int_A \frac{1}{2}\left(\sigma_{\alpha\beta}^{(1)}\frac{\partial\varepsilon_{\alpha\beta}^{(2)}}{\partial x_1'} - \frac{\partial\sigma_{\alpha\beta}^{(2)}}{\partial x_1'}\varepsilon_{\alpha\beta}^{(1)} + \sigma_{\alpha\beta}^{(2)}\frac{\partial\varepsilon_{\alpha\beta}^{(1)}}{\partial x_1'} - \frac{\partial\sigma_{\alpha\beta}^{(1)}}{\partial x_1'}\varepsilon_{\alpha\beta}^{(2)}\right)qdA \end{aligned} \tag{15}$$

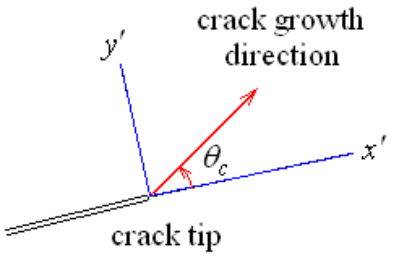

Fig. 4 The critical angle indicating the crack growth direction

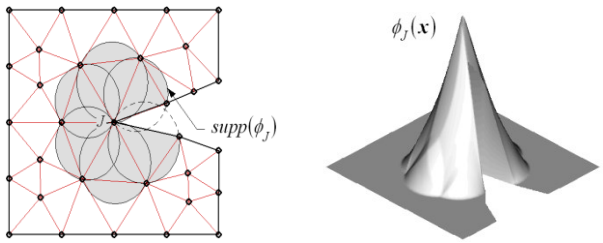

(a) (b)

Fig. 5 (a) Cracked NEM grid, (b) crack-tip L/I function $\varphi_J(\boldsymbol{x})$

denotes the modified interaction integral (Gu *et al.* 1999).

The above two $J-$integrals (13) and (14) for linearly elastic heterogeneous body under mixed modes I and II do also represent the energy release rates, so those become

$$J^{(1)} = \frac{1}{\bar{E}_{tip}}\left(K_I^{(1)^2} + K_{II}^{(1)^2}\right) \tag{16}$$

$$J^{(2)} = \frac{1}{\bar{E}_{tip}}\left(K_I^{(2)^2} + K_{II}^{(2)^2}\right) \tag{17}$$

and thus

$$J^{(S)} = J^{(1)} + J^{(2)} + \frac{2}{\bar{E}_{tip}}\left(K_I^{(1)}K_I^{(2)} + K_{II}^{(1)}K_{II}^{(2)}\right) \tag{18}$$

Here, $\bar{E}_{tip}$ becomes E_{tip} for the state of plane stress and $E_{tip}/(1-\nu^2)$ for the state of plane strain with E_{tip} being the crack-tip elastic modulus and ν being the Poisson's ratio. By equating Eq. (12) with Eq. (18), one obtain (Dolbow and Gosz 2002)

$$M^{(1,2)} = \frac{2}{\bar{E}_{tip}}\left(K_I^{(1)}K_I^{(2)} + K_{II}^{(1)}K_{II}^{(2)}\right) \tag{19}$$

The closed form crack-tip displacement and stress fields for modes I and II in 2-D linear fracture mechanics are accessible (Cho and Lee 2014). Thus, the SIF $K_I^{(1)}$ for mode I is determined by letting state 2 be the asymptotic field of mode I (i.e., $K_I^{(2)} = 1$ and $K_{II}^{(2)} = 0$):

$$M^{(1,\text{Mode I})} = \frac{2}{\bar{E}_{tip}}K_I^{(1)} \tag{20}$$

In the same manner, the SIF K_{II} for mode II is also determined.

Regarding the criterion for determining the crack propagation direction depicted in Fig. 4, there are three representative criterions based on (i) the maximum energy release rate (MERR), (ii) the maximum principal stress (MPS) and (iii) the minimum strain energy density (MSED) (Pant *et al.* 2013). In this study, the MPS criterion is adopted, in which crack grows in the direction of maximum circumferential stress $\sigma_{\theta\theta}$. Therefore, according to this criterion, the crack propagation direction is identical to the principal axis. Because the asymptotic crack-tip shear stress in mixed-mode loading is given by (Pant *et al.* 2013)

$$\sigma_{r\theta} = \frac{K_I}{4\sqrt{2\pi r}}\left[sin\left(\frac{\theta}{2}\right) + sin\left(\frac{3\theta}{2}\right)\right] + \frac{K_{II}}{4\sqrt{2\pi r}}\left[cos\left(\frac{\theta}{2}\right) + 3\,cos\left(\frac{3\theta}{2}\right)\right] \tag{21}$$

the critical angle θ_c has to obey the following relation given by

$$K_I\,sin(\theta_c) + K_{II}(3cos(\theta_c) - 1) = 0 \tag{22}$$

Hence, the critical angle θ_c is determined according to

$$\theta_c = 2\,arctan\frac{1}{4}\left(K_I / K_{II} \pm \sqrt{(K_I / K_{II})^2 + 8}\right) \tag{23}$$

Next, whether the crack will be advanced or not should be determined by comparing the equivalent mode-I SIF K_{Ieqv} (Pant *et al* 2013) which is calculated by

$$K_{Ieqv} = K_I\,cos^3\left(\frac{\theta_c}{2}\right) - 3K_{II}\,cos^2\left(\frac{\theta_c}{2}\right)sin\left(\frac{\theta_c}{2}\right) \tag{24}$$

with the fracture toughness K_{Ic} of the heterogeneous FG structure. The crack will propagate only when K_{Ieqv} is greater than K_{Ic}.

4. Enriched Petrov-Galerkin natural element method

By virtue of virtual work principle, the BVP governed by Eqs. (7)-(9) is switched to the next variational formulation: Find $\boldsymbol{u}(\boldsymbol{x})$ such that

$$\int_\Omega \varepsilon(\boldsymbol{v}) : \sigma(\boldsymbol{u})\,d\Omega = \int_{\Gamma_N} \hat{\boldsymbol{t}} \cdot \boldsymbol{v}\,ds \tag{25}$$

For all the possible virtual displacement fields $\boldsymbol{v}(\boldsymbol{x})$ in the Cartesian coordinates $\{x, y\}$. The non-convex material domain Ω is discretized into a NEM grid composed of N nodes and M Delaunay triangles, as represented in Fig. 5(a). And, in the enriched Petrov-Galerkin NE approximation, the actual displacement $\boldsymbol{u}(\boldsymbol{x})$ and the virtual displacement $\boldsymbol{v}(\boldsymbol{x})$ are expressed by (Cho 2019)

$$\boldsymbol{u}_h(\boldsymbol{x}) = \sum_{J=1}^{N}\bar{\boldsymbol{u}}_J\phi_J(\boldsymbol{x}) + k_1\begin{bmatrix}S_{11}(\boldsymbol{x})\\S_{12}(\boldsymbol{x})\end{bmatrix} + k_2\begin{bmatrix}S_{21}(\boldsymbol{x})\\S_{22}(\boldsymbol{x})\end{bmatrix} \tag{26}$$

$$\boldsymbol{v}_h(\boldsymbol{x}) = \sum_{I=1}^{N}\bar{\boldsymbol{v}}_I\Psi_I(\boldsymbol{x}) + \lambda_1\begin{bmatrix}S_{11}(\boldsymbol{x})\\S_{12}(\boldsymbol{x})\end{bmatrix} + \lambda_2\begin{bmatrix}S_{21}(\boldsymbol{x})\\S_{22}(\boldsymbol{x})\end{bmatrix} \tag{27}$$

In which $\varphi_J(\boldsymbol{x})$ are L/I functions shown in Fig. 5(b),

while $\psi_I(\boldsymbol{x})$ denote Delaunay triangle-based constant strain FE basis functions.

In addition, k_1 and k_2 indicate the enrichment constants to be approximated, and $S_{1\alpha}(\boldsymbol{x})$ and $S_{2\alpha}(\boldsymbol{x})$ denote the singular functions defined by (Cho 2019)

$$S_{11}(\boldsymbol{x})=\frac{1}{2\mu}\sqrt{\frac{r}{2\pi}}\cos(\hat{\theta})\left[\kappa-1+2\sin^2(\hat{\theta})\right] \tag{28}$$

$$S_{12}(\boldsymbol{x})=\frac{1}{2\mu}\sqrt{\frac{r}{2\pi}}\sin(\hat{\theta})\left[\kappa+1-2\cos^2(\hat{\theta})\right] \tag{29}$$

$$S_{21}(\boldsymbol{x})=\frac{1}{2\mu}\sqrt{\frac{r}{2\pi}}\sin(\hat{\theta})\left[\kappa+1+2\cos^2(\hat{\theta})\right] \tag{30}$$

$$S_{22}(\boldsymbol{x})=\frac{-1}{2\mu}\sqrt{\frac{r}{2\pi}}\cos(\hat{\theta})\left[\kappa-1-2\sin^2(\hat{\theta})\right] \tag{31}$$

with $\hat{\theta}=\theta/2$. Where, $\{r,\theta\}$ is the polar coordinates which is originated at the crack tip, referring to Fig. 1(a). In addition, μ and κ denote the shear modulus and the Kolosov constant given by

$$\kappa=\begin{cases}3-4\nu & \text{plane strain}\\ (3-\nu)/(1+\nu) & \text{plane stress}\end{cases} \tag{32}$$

with the Poisson's ratio ν. Using Eq. (26), the global nodal coefficients $\bar{\boldsymbol{u}}_{\boldsymbol{J}}$ are calculated as

$$\bar{\boldsymbol{u}}_J(\boldsymbol{x})=\boldsymbol{u}_h(\boldsymbol{x}_J)-k_1\begin{bmatrix}S_{11}(\boldsymbol{x}_J)\\ S_{12}(\boldsymbol{x}_J)\end{bmatrix}-k_2\begin{bmatrix}S_{21}(\boldsymbol{x}_J)\\ S_{22}(\boldsymbol{x}_J)\end{bmatrix} \tag{33}$$

and the global stresses and strains corresponding to $\bar{\boldsymbol{u}}_{\boldsymbol{J}}$ are smoothened by the strain recovery technique. Meanwhile, the original displacement boundary condition (8) is changed to

$$\hat{\boldsymbol{u}}=\hat{\boldsymbol{u}}-k_1\begin{bmatrix}S_{11}(\hat{\boldsymbol{x}})\\ S_{12}(\hat{\boldsymbol{x}})\end{bmatrix}-k_2\begin{bmatrix}S_{21}(\hat{\boldsymbol{x}})\\ S_{22}(\hat{\boldsymbol{x}})\end{bmatrix},\quad \hat{\boldsymbol{x}}\quad on\quad \Gamma_D \tag{34}$$

By plugging Eqs. (26) and (27) into Eq. (25), it is not hard to get

$$\begin{bmatrix}\boldsymbol{K}_{IJ} & K_{I1} & K_{I2}\\ K_{I1}^T & K_{11} & K_{12}\\ K_{I2}^T & K_{12}^T & K_{22}\end{bmatrix}\begin{Bmatrix}\bar{\boldsymbol{u}}_J\\ k_1\\ k_2\end{Bmatrix}=\begin{Bmatrix}\boldsymbol{F}_I\\ f_1\\ f_2\end{Bmatrix} \tag{35}$$

In which the global stiffness matrix $\boldsymbol{K}_{IJ}$ and load vector $\boldsymbol{F}_I$ are calculated as

$$\boldsymbol{K}_{IJ}=\int_\Omega \boldsymbol{B}_I^T\boldsymbol{D}\boldsymbol{B}_J\,d\Omega,\quad \boldsymbol{F}_I=\int_{\Gamma_N}\Phi_I^T\hat{\boldsymbol{t}}\,ds \tag{36}$$

With

$$\boldsymbol{B}_I^T=\begin{bmatrix}\phi_{I,x} & 0 & \phi_{I,y}\\ 0 & \phi_{I,y} & \phi_{I,x}\end{bmatrix} \tag{37}$$

$$\boldsymbol{D}=\frac{E}{(1+\nu)(1-2\nu)}\begin{bmatrix}1-\nu & \nu & 0\\ \nu & 1-\nu & 0\\ 0 & 0 & \dfrac{1-2\nu}{2}\end{bmatrix} \tag{38}$$

for the state of plane strain. And, the enrichment stiffness matrix $K_{\alpha\beta}$, the associated load vector f_α, and the interface matrix $K_{I\alpha}$ are defined by, respectively

$$K_{\alpha\beta}=\int_\Omega \hat{\boldsymbol{B}}_\alpha^T\boldsymbol{D}\hat{\boldsymbol{B}}_\beta\,d\Omega,\ f_\alpha=\int_{\Gamma_N}\hat{\phi}_\alpha^T\hat{\boldsymbol{t}}ds,\quad \alpha,\beta=1,2 \tag{39}$$

$$K_{I\alpha}=\int_\Omega \boldsymbol{B}_I^T\boldsymbol{D}\hat{\boldsymbol{B}}_\alpha\,d\Omega \tag{40}$$

With

$$\hat{\phi}_\alpha^T=\left[Q_{\alpha1}(\boldsymbol{x}),Q_{\alpha2}(\boldsymbol{x})\right] \tag{41}$$

$$\hat{\boldsymbol{B}}_\alpha=\begin{bmatrix}Q_{\alpha\alpha,x}(\boldsymbol{x})\\ Q_{\alpha\beta,y}(\boldsymbol{x})\\ Q_{\alpha\alpha,y}(\boldsymbol{x})+Q_{\alpha\beta,y}(\boldsymbol{x})\end{bmatrix},\quad \alpha\alpha=\text{no sum} \tag{42}$$

The previous work (Cho and Lee 2014) would be referable for more detailed explanation about the integration domain A and the weighting function $q(\boldsymbol{x})$.

5. Numerical experiments

The numerical formula described in Section 4 were coded in Fortran and integrated into the previously developed PG-NEM test program (Cho and Lee 2006, 2014). The numerical simulation procedure of crack growth in heterogeneous FG porous plates by the proposed method is conducted as follows:

i) Generate an initial NEM grid for cracked heterogeneous FG porous plate.

ii) Perform the structural analysis by the developed enriched PG-NEM program.

iii) Perform the global strain recovery to improve strain and stress fields (Cho 2016).

iv) Perform the modified interaction integral $M^{(1,2)}$ in Eq. (15) triangle by triangle.

v) Calculate two SIFs K_I and K_{II} using Eq. (20).

vi) Calculate the critical angle θ_c using Eq. (24).

vii) Calculate the equivalent mode-I SIF K_{Ic} using Eq. (25).

viii) If $K_{Ieqv}>K_{Ic}$, then advance the crack using the angle θ_c and the crack-tip node.

ix) Adapt the current NEM grid for the next crack analysis, and go to the next iteration.

x) If not, terminate the simulation.

Fig. 6(a) shows a rectangular plate in the plane-strain state taken for the numerical experiments where the detailed values are dependent of the simulation problem. Fig. 6(b) illustrates a uniform cracked NEM grid used for the numerical simulation. The structural analysis by the

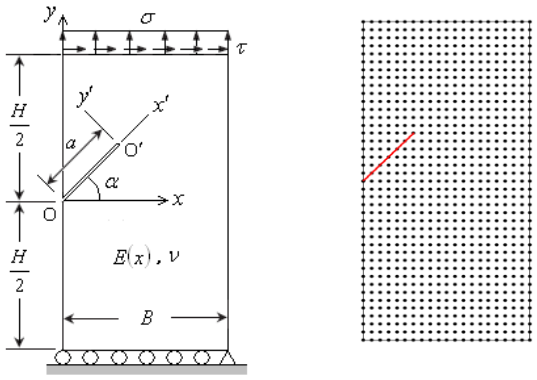

(a) (b)

Fig. 6 A rectangular plate having an edge crack subject to uniform distributed loads: (a) geometry, (b) cracked NEM grid

Table 1 Material properties of metal and ceramic components

Items	Young's modulus $E(GPa)$	Poisson's ratio ν	Fracture toughness $K_{Ic}(MPa\cdot\sqrt{m})$
Ni	200	0.25	96
Al₂O₃	400	0.25	4

enriched PG-NEM was performed with 7 Gauss points.

First, the crack propagation of a horizontal edge crack shown in Fig. 7(a) within an isotropic plate with $H = 0.2\ m$ and the width $W = 0.1\ m$ is considered. The elastic modulus and Poisson's ratio are $E = 200GPa$ and $\nu = 0.3$. The initial crack length is 0.02m. The plate bottom is simply supported while the top side is loaded by the uniformly distributed tension $\sigma = 50MPa$ and shear $\tau = 25MPa$. The density of uniform NEM grid is chosen by 18×35. One can see from Fig. 7(b) that the present result is in good agreement with one by Pant *et al.* (2013).

Second, a ceramic-metal (*Al₂O₃-Ni*) homogenized rectangular plate is considered, where the volume fractions of *Ni* and *Al₂O₃* are 50% and 50%. The material properties given in Table 1 of two base materials are set by referring to Jin and Batra (1996). The plate size is $B = 7\ m$ and $B = 16\ m$, and the length and the angle of initial edge crack are $2.1\ m$ and 0^o, respectively. The plate bottom is perfectly clamped and the plate top is loaded by uniform distributed shear $\tau = 5.0MPa$. The density of uniform NEM grid is chosen by 21×41. According to the linear rule of mixtures (Cho and Oden 2000), the equivalent elastic modulus E and the fracture toughness K_{Ic} are determined as $300.0GPa$ and $50Mpa \cdot m^{1/2}$. For the sake of comparison, the example was also solved by ANSYS (2019) with a locally refined FEM mesh which was generated with total 197,800 4-node elements.

The crack growth trajectory obtained by the present method is presented in Fig. 8(a), and it is compared with ANSYS in Fig. 8(b). It is seen that the crack growth direction coincides well with one of ANSYS. It was found that the propagation angles by the present method and ANSYS are 51.6^o and 50^o. Thus, the relative differences

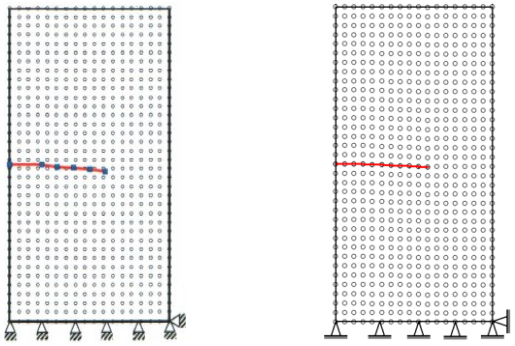

(a) (b)

Fig. 7 The comparison of edge crack propagation: (a) Pant *et al.* (2013), (b) present

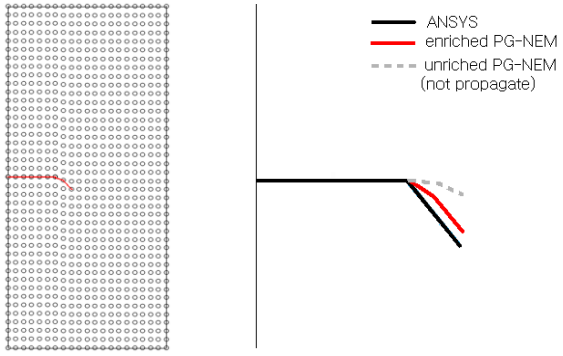

(a) (b)

Fig. 8 Crack propagation in the homogenized plate: (a) the present enriched PG-NEM, (b) ANSY

between the present method and ANSYS are 3.2% in the crack angle and 5.3% in the crack length.

For the further comparison purpose, the crack growth was simulated without using the enrichment, and the detailed numerical values are compared in Table 2. Differing from the enriched method, the unriched method predicts the remarkably lower propagation angle equal to 23.9^o. Moreover, it predicts that the edge crack does not advence from the fact that K_{Ieqv} is lower than the fracture toughness $K_{Ic} = 50$. Consequently, the reliability of present method was verified such that the maximum relative difference in the crack propagation is lower than 6%.

Third, the crack growth in heterogeneous *Al₂O₃ -Ni* FG plate obeying the exponential variation given in the previous Eq. (4) is parametrically investigated with regard to the elastic modulus index η. The previous rectangular plate with a horizontal edge crack is chosen by keeping the geometry dimensions and the simulation parameters unchanged, except for the elastic modulus and the fracture toughness. The effective elastic modulus $E(x)$ is determined according to Eq. (4), and similarly the fracture toughness K_{Ic} is expressed as

$$K_{Ic}(x) = K_{Ic,Al_2O_3}\ exp\left(\frac{3.18\eta x}{B}\right), \quad \eta \geq 0 \tag{43}$$

To meet K_{Ic,Al_2O_3} at the left side and $K_{Ic,Ni}$ at the right

Table 2 The comparison of crack propagation between with and without enrichment

Enrichment	Initial				Second				Total angle
	K_I	K_{II}	θ_c	K_{Ieqv}	K_I	K_{II}	θ_c	K_{Ieqv}	$\bar{\theta}_c$
With	52.11	11.49	-22.90	55.63	50.76	14.96	-28.70	56.59	-51.60
Without	40.93	2.32	(-6.40)	41.12	41.97	6.93	(-17.50)	42.07	(-23.90)

Table 3 The effect of elastic modulus index η on the crack trajectory

η	Initial				Final				# of steps	Total angle
	K_I	K_{II}	θ_c	$K_{Ieqv}(K_{Ic})$	K_I	K_{II}	θ_c	$K_{Ieqv}(K_{Ic})$		$\bar{\theta}_c$
0.25	11.806	0.672	-6.50	11.86 (5.08)	Fracture					
0.5	11.704	0.510	-5.00	11.73 (6.44)	8.148	2.213	-27.00	8.96 (8.18)	5	-56.60
0.75	11.580	0.354	-3.50	11.59 (8.18)	9.918	2.145	-22.50	10.56 (10.38)	3	-31.90
1.0	11.435	0.206	-2.10	11.44 (10.38)	13.636	1.221	-10.10	13.79 (12.17)	2	-12.20

(*) indicate the crack-tip fracture toughness

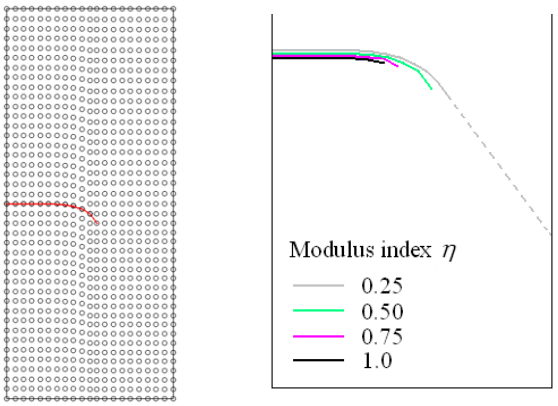

(a) (b)

Fig. 9 Crack propagation within the ceramic-metal FG plate (a) at $\eta = 0.5$, (b) effect of η on the crack trajectory

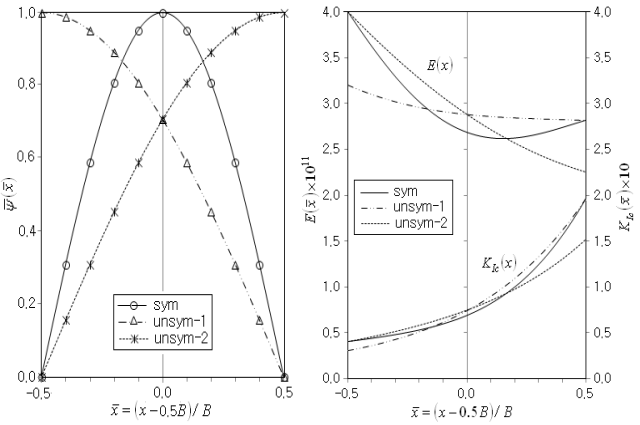

(a) (b)

Fig. 10 Porous FG plate: (a) three porosity distributions, (b) variations of $E(x)$ and $K_{Ic}(x)$ $(\eta = 0.5, \vartheta = 0.2)$

side. The external loading at the top side is changed to a combination of distributed loads $\sigma = 5.0MPa$ and $\tau = 1.0MPa$. As in the previous example, a uniform 21×41 NEM grid is chosen and 7 Gauss points are taken for the structural analysis, the strain recovery and the modified $M^{(1,2)}$ interaction integral. The propagation simulation was performed for four different values of η, as presented in Table 3, to investigate the effect of η.

For the initial crack, the mixed-mode SIFs K_I and K_{II} and the critical angle θ_c uniformly decrease proportional to the elastic modulus index η. But, this uniform variation is not seen any longer at the second state. The crack trajectory becomes longer with the decrease of η such that the crack completely penetrates the plate when η becomes or less than 0.25. It is because the fracture toughness K_{Ic} decreases in reverse proportion to η.

Fig. 9(a) represents the crack trajectory when η is 0.5, and which was obtained in five increments of crack advancement, as presented in Table 3. Compared to the homogenized case shown in Fig. 8(a), the critical angle θ_c is similar but the trajectory becomes longer. Fig. 9(b) comparatively represents the crack trajectories for different values of η, where the dotted graph of $\eta = 0.25$ was plotted using the crack growth slopes at previous stages. It is seen that the crack propagation length is strongly influenced by the elastic modulus index η, but the crack growth direction is not affected by this index. It is because the elastic modulus index η remarkably influences the fracture toughness but its influence on the ratio K_I/K_{II} is not remarkable. As a result, this parametric result suggests that the crack trajectory within the ceramic-metal FG plate can be adjusted by changing the spatial gradient of elastic modulus and fracture toughness.

Next, the proposed enriched numerical method is applied to the ceramic-metal FG porous plate in which the porosity is distributed in the horizontal direction, as addressed in Section 2. Three different porosity distributions are comparatively represented in Fig. 10(a) for $\vartheta = 0.2$, where unsym-1 is biased towards the left while one in unsym-2 leans towards the right. Fig. 10(b) compares the resulting distributions of the effective elastic modulus E and the fracture stiffness K_{Ic} which were compued acciodring to Eqs. (5) and (6).

Backing to Fig. 6(a), the edge crack is inclined by 45^0 so that the initial crack length is changed to $2.1\sqrt{2}m$ while

Table 4 The crack propagation trajectories for different porosity distributions ($\eta = 0.5, \vartheta = 0.2$)

Porosity pattern	Initial				Final				# of steps	Total angle
	K_I	K_{II}	θ_c	$K_{Ieqv}(K_{Ic})$	K_I	K_{II}	θ_c	$K_{Ieqv}(K_{Ic})$		$\tilde{\theta}_c$
Sym	7.747	5.029	-45.57	11.04 (5.26)	6.909	-0.489	-8.01	6.96(6.85)	5	-22.58
Unsym-1	8.107	4.852	-43.95	11.15 (5.14)	10.352	-0.489	-5.38	10.39(8.99)	7	-34.76
Unsym-2	7.771	5.098	-45.78	11.12 (5.78)	9.021	-0.639	-8.02	9.09(7.43)	5	-26.47
Non-porous	8.395	4.768	-42.90	11.30 (6.44)	10.963	-0.353	-3.70	10.98(8.14)	4	-11.70

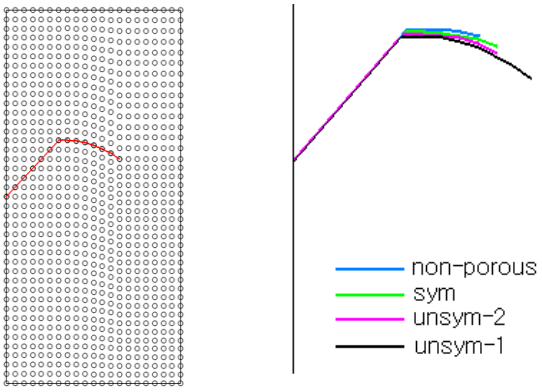

(a) (b)

Fig. 11 Crack propagation within the ceramic-metal FG porous plate ($\eta = 0.5, \vartheta = 0.2$) (a) for the unsym-1 porosity distribution, (b) influence of the porosity distribution

the other geometry dimensions are kept the same with the previous case. The plate bottom is simply supported while the top side is subjected to a combination of normal traction $\sigma = 0.5MPa$ and shear $\tau = 0.25MPa$. The numerical results of crack propagation in the ceramic-metal FG porous plates are presented in Table 4, where the case of non-porous plate is also given for the comparison purpose.

And, the crack trajectories are comparatively represented in Fig. 11.

First of all, it is seen that the crack growth lengths in the ceramic-metal FG porous plates are longer than one in the non-porous case. It is because both the stiffness and fracture toughness of porous plate is lower than ones of non-porous plate. Regarding the porous FG plates, the unsym-1 distribution leads to the longest crack growth because both the elastic modulus and the fracture stiffness in the left region are lower than the other two distribution cases. Meanwhile, the sym and unsym-2 distributions do not show the remarkable difference because these two distributions show similar distributions of E and K_{Ic} in the left region. Regarding the crack propagation direction, the existence of porosity and the porosity distribution do not produce any remarkable difference. It is because the porosity is graded in the horizontal direction which is almost similar to the crack growth direction.

6. Conclusions

In this paper, the crack propagation within the ceramic-metal FG porous plates is simulated and investigated by the enriched PG-NEM. The displacement was approximated and enriched by making use of L/I functions and the crack-tip singular field. The mixed-mode SIFs at the crack tip were extracted from the modified $M^{(1,2)}$ -interaction integral. The critical crack angle was determined by adopting the MPS criterion, and the crack trajectory was obtained by marching the crack-tip node in the direction of critical crack angle.

The numerical experiments were conducted to demonstrate the proposed method and the crack propagation results were compared with the unriched PG-NEM and ANSYS. Moreover, the crack growth characteristics were investigated with respect to the volume fractions and the porosity distribution pattern. The numerical results draw the next major observations:

1. Compared to ANSYS, the unriched method leads to no crack propagation with much smaller crack critical angle. But, the proposed enriched PG-NEM provides the numerical results which coincide well with ANSYS, such that relative difference in the propagation angle and length is lower than 6.0%, justifying the reliability of present method.

2. For the ceramic-metal FG plates with the exponentially varying Young's modulus, the trajectory length becomes longer in reverse proportion to the elastic modulus index η. It is because the plate becomes more dominated by ceramic with lower fracture toughness.

3. In the case of porous FG plate, the crack growth length is remarkably influenced by the porosity distribution pattern but the crack growth direction is not. The unsym-2 leads to the longest crack trajectory while the sym and unsym-1 show the crack propagations similar to each other.

Meanwhile, the present method is limited to rather simple crack configuration owing to the painstaking crack generation and crack adaption in grid-based 2-D NEM method. Hence, a more effective method, such as a phase-field formulation (Doan *et al.* 2017, Minh *et al.* 2018), would be adopted, and which would deserve a valuable research topic for future work.

Acknowledgements

This work was supported by the National Research Foundation of Korea (NRF) grant funded by the Korea government (MSIT) (RS-2023-00240618).

References

Abdelaziz, H.H., Meziane, M.A., Bousahla, A.A., Tounsi, A., Mahmoud, S.R. and Alwabli, A.S. (2017) "An efficient hyperbolic shear deformation theory for bending, buckling and free vibration of FGM sandwich plates with various boundary conditions", *Steel Comp. Struct*., **25**(6), 693-704. https://doi.org/10.12989/scs.2017.25.6.693.

Anlas, G., Santare, M.H. and Lambros, J. (2000) "Numerical calculation of stress intensity factors in functionally graded materials", *Int. J. Fracture*, **104**, 131-143. https://doi.org/10.1023/A:1007652711735.

ANSYS (2019), *Users' Manual, Ver. 19.0*, USA.

Apalak, M.K. (2014) "Functionally graded adhesively bonded joints", *Rev. Adhesion Adhesive*., **1**, 56-84. https://doi.org/10.7569/RAA.2014.097301.

Atkinson, C. and List, R.D. (1978) "Steady state crack propagation into media with spatially varying elastic properties", *Int. J. Eng. Sci*., **16**, 717-730. https://doi.org/10.1016/0020-7225(78)90006-X.

Ayhan, A.O. (2009) "Three-dimensional mixed-mode stress intensity factors for cracks in functionally graded materials using enriched finite elements", *Int. J. Solids Struct.,* **46**(3-4), 796-810. https://doi.org/10.1016/j.ijsolstr.2008.09.026.

Birman, V. and Byrd, L.W. (2007) "Modeling and analysis of functionally graded materials and structures", *Appl. Mech. Rev*., **60**(5), 195-216. https://doi.org/10.1115/1.2777164.

Bouderba, B. (2018) "Bending of FGM rectangular plates resting on non-uniform elastic foundations in thermal environmental using an accurate theory", *Steel Composite Struct.,* **27**(3), 311-325. https://doi.org/10.12989/scs.2018.27.3.311.

Cho, J.R. (2016) "Stress recovery techniques for natural element method in 2-D solid mechanics", *J. Mech. Sci. Technol.,* **30**(11), 5083-5091. https://doi.org/10.1007/s12206-016-1026-4.

Cho, J.R. (2019) "A numerical evaluation of SIFs of 2-D functionally graded materials by enriched natural element method", Appl. Sci., 9, 3581. https://doi.org/10.3390/app9173581.

Cho, J.R. and Ha, D.Y. (2001) "Averaging and finite-element discretization approaches in the numerical analysis of functionally graded materials", *Mater. Sci. Eng. A*, **302**, 187-196. https://doi.org/10.1016/S0921-5093(00)01835-9.

Cho, J.R. and Lee, H.W. (2006) "A Petrov-Galerkin natural element method securing the numerical integration accuracy", *J. Mech. Sci. Technol*., **20**(1), 94-109. https://doi.org/10.1007/BF02916204.

Cho, J.R. and Lee, H.W. (2014) "Calculation of stress intensity factors in 2-D linear fracture mechanics by Petrov–Galerkin natural element method", *Int. J. Numer. Methods Engng.,* **98**, 819-839. https://doi.org/10.1002/nme.4666.

Cho, J.R. and Oden, J.T. (2000) "Functionally graded material: a Parametric study on thermal stress characteristics using the Crank-Nicolson-Galerkin scheme", *Comput. Method. Appl. Mech. Engrg*., **188**, 17-38. https://doi.org/10.1016/S0045-7825(99)00289-3.

Delale, F. and Erdogan, F. (1983) "The crack problem for a nonhomogeneous plane", *J. Appl. Mech*., **50**, 609-614. https://doi.org/10.1115/1.3167098.

Ding, S. and Wu, C.P. (2018) "Optimization of material composition to minimize the thermal stresses induced in FGM plates with temperature-dependent material properties", *Int. J. Mech. Mater.*, 14, 527-549. https://doi.org/10.1007/s10999-017-9388-z.

Doan, D.H., Bui, T.Q., Van Do, T. and Duc, N.D. (2017) "A rate-dependent hybrid phase field model for dynamic crack propagation", *J. Appl. Phys.*, **122**, 115102. https://dx.doi.org/10.1063/1.4990073.

Dolbow, J.E. and Gosz, M. (2002) "On the computation of mixed-mode stress intensity factors in functionally graded materials", *Int. J. Solids Struct*., **39**(9), 2557-2574. https://doi.org/10.1016/S0020-7683(02)00114-2.

Duc, N.D. and Minh, P.P. (2021) "Free vibration analysis of cracked FG CNTRC plates using phase field theory", *Aero. Sci. Technol*., **112**, 106654. https://doi.org/10.1016/j.ast.2021.106654.

Eischen, J.W. (1987) "Fracture of nonhomogeneous materials", *Int. J. Fracture*, **34**, 3-22. https://doi.org/10.1007/BF00042121.

Fleming, M., Chu, Y.A., Moran, B., Belytschko, T. (1997) "Enriched element-free Galerkin methods for crack tip fields", *Int. J. Numer. Methods Engng*., **40**, 1483-1504. https://doi.org/10.1002/(SICI)1097-0207(19970430)40:8<1483:: AID-NME123>3.0.CO;2-6.

Flinn, B.D., Bordia, R.K., Zimmermann, A. and Rödel, J. (2000) "Evolution of defect size and strength of porous alumina during sintering", *J. Eur. Ceram. Soc*., **20**(14-15) 2561-2568. https://doi.org/10.1016/S0955-2219(00)00133-3.

Giannakopulos, A.E., Suresh, S., Olsson, M. (1995) "Elastoplastic analysis of thermal cycling: layered materials with compositional gradients", *Acta Metall. Mater*., **43**(4), 1335-1354. https://doi.org/10.1016/0956-7151(94)00360-T.

Gu, P., Dao, M. and Asaro, R.J. (1999) "A simplified method for calculating the crack tip field of functionally graded materials using the domain integral", *J. Appl. Mech*., **66**(1), 101-108. https://doi.org/10.1115/1.2789135.

Ivanov, I.V., Sadowski, T., Pietras, D. (2013) "Crack propagation in functionally graded strip under thermal shock", *Europ. Phys. J. Special Topics*, **222**(7), 1587-1595. https://doi.org/10.1140/epjst/e2013-01947-3.

Jin, Z.H. and Batra, R.C. (1996) "Some basic fracture mechanics concepts in functionally graded materials", *J. Mech. Phys. Solids,* **44**(8), 1221-1235. https://doi.org/10.1016/0022-5096(96)00041-5.

Khiem, N.T., Hai, T.T. and Huong, L.Q. (2023) "Modal analysis of cracked FGM beam with piezoelectric layer", *Mech. Based Des. Struct. Mach*., **51**(9), 5120-5140. https://doi.org/10.1080/15397734.2021.1992775.

Kim, J.H. and Paulino, G.H. (2002) "Finite element evaluation of mixed mode stress intensity factors in functionally graded materials", *Int. J. Numer. Methods Engng*., **53**, 1903-1935. https://doi.org/10.1002/nme.364.

Kumar, P., Sharma, S.K. and Singh, R.K.R. (2023), "Recent trends and future outlooks in manufacturing methods and applications of FGM: a comprehensive review", *Mater. Manufac. Proc*., **38**(9), 1033-1067. https://doi.org/10.1080/10426914.2022.2075892.

Liu, K.Y., Long, S.Y. and Li, G.Y. (2008) "A meshless local Petrov-Galerkin method for the analysis of cracks in the isotropic functionally graded material", *Comput. Modeling Eng. Sci.*, **7**(1), 43-57.

Mahamood, R.M., Akinlabi, E.T., Shukla, M., Pityana, S. (2012) "Functionally graded material: An overview", *Proc. World Congress Eng. (WCE 2012)*, London, UK.

Minh, P.P., Duc, N.D. (2021) "The effect of cracks and thermal environment on free vibration of FGM plates", *Thin-Wall. Struct*., **159**, 107291. https://doi.org/10.1016/j.tws.2020.107291.

Minh, P.P.; Van Do, T., Hong Duc, D. and Duc, N.D. (2018) "The stability of cracked rectangular plate with variable thickness using phase field method", *Thin-Wall. Struct*., **129**, 157-165. https://doi.org/10.1016/j.tws.2018.03.028.

Miyamoto, Y., Kaysser, W.A., Rabin, B.H. and Kawasaki, A. (2013) *Functionally Graded Materials: Design. Processing and Applications*, Springer Science & Business Media.

Nguyen, D.D., Nguyen, M.N., Duc, N.D. and Bui, T.Q. (2022), "Modeling the transient dynamic fracture and quasi-static crack

growth in cracked functionally graded composites by the extended four-node gradient finite elements", *Compos. Struct*., **284**, 115056. https://doi.org/10.1016/j.compstruct.2021.115056.

Nikishkov, G.P., Vershinin, A.V., Nikishkov, Y.G. (2016), "Mesh-independent equivalent domain integral methof for J-integral evaluation", *Adv. Eng. Softw*., 100, 308-318. https://doi.org/10.1016/j.advengsoft.2016.08.006.

Pant, M., Singh, I.V. and Mishra, B.K. (2013), "A novel enrichment criterion for modeling kinked cracks using element free Galerkin method", *Int. J. Mech. Sci*., **68**, 140-149. https://doi.org/10.1016/j.ijmecsci.2013.01.008.

Pham, P.M. and Nguyen Dinh, D. (2023), "Free vibration of cracked MEE plates resting on elastic foundations using phase-field simulation", *J. Eng. Mech*., **149**(11), https://doi.org/10.1061/JENMDT.EMENG-7088.

Phani, K.K. and Niyogi, S.K. (1987), "Young's modulus of porous brittle solids", *J. Mater. Sci*., **22**, 257-263, https://doi.org/10.1007/BF01160581.

Rao, B.N. and Rahman, S. (2003), "Mesh-free analysis of cracks in isotropic functionally graded materials", *Eng. Fracture Mech*., **70**, 1-27. https://doi.org/10.1016/S0013-7944(02)00038-3.

Reiter, T. and Dvorak, G.J. (1998), "Micromechanical models for graded composite materials: II. Thermomechanical loading", *J. Phys. Solids*, **46**(9), 1655-1673. https://doi.org/10.1016/S0022-5096(97)00039-2.

Sukumar, N., Moran, A. and Belytschko, T. (1998), "The natural element method in solid mechanics", *Int. J. Numer. Methods Engng*., **43**, 839-887. https://doi.org/10.1002/(SICI)1097-0207(19981115)43:5<839::AID-NME423>3.0.CO;2-R.

Tilbrook, M.T., Moon, R.J. and Hoffman, M. (2005) "Crack propagation in graded composites", *Composite Sci. Technol*., **65**(2), 201-220. https://doi.org/10.1016/j.compscitech.2004.07.004.

Van Do, T., Hong Doan, D., Chi Tho, N. and Duc, N.D. (2022) "Thermal buckling analysis of cracked functionally graded plates", *Int. J. Struct. Stab. Dyn*., **22**(8), 2250089. https://doi.org/10.1142/S0219455422500894.

Yahia, S.A., Atmane, H.A., Houari, M.S.A. and Tounsi, A. (2015), "Wave propagation in functionally graded plates with porosities using various higher-order shear deformation plate theories", *Struct. Eng. Mech.*, **53**(6), 1143-1165. https://doi.org/10.12989/sem.2015.53.6.1143.

Zhang, Ch., Sladek, J. and Sladek, V. (2004), "Crack analysis in unidirectionally and bidirectionally functionally graded materials", *Int. J. Fracture*, **129**, 385-406. https://doi.org/10.1023/B:FRAC.0000049495.13523.94.

Zhu, X.K. (2023) "Effects of large plastic deformation and residual stress on the path independence of J-integral for cracks in ductile materials", *Eng. Fract. Mech*., **277**, 108945. https://doi.org/10.1016/j.engfracmech.2022.108945.